# Efficient Modeling of Infinite Scatterers Using a Generalized Total-Field/Scattered-Field FDTD Boundary Partially Embedded Within PML

Veeraraghavan Anantha and Allen Taflove, *Fellow, IEEE*

*Abstract*—This paper proposes a novel generalized total-field/scattered-field (G-TF/SF) formulation for finite-difference time-domain (FDTD) to efficiently model an infinite material scatterer illuminated by an arbitrarily oriented plane wave within a compact FDTD grid. This requires the sourcing of numerical plane waves traveling into, or originating from, the perfectly matched layer (PML) absorber bounding the grid. In this formulation, the G-TF/SF wave source boundary is located in part within the PML. We apply this technique to efficiently model two-dimensional (2-D) transverse-magnetic diffraction of an infinite right-angle dielectric wedge and an infinite 45°-angle perfect-electrical-conductor wedge. This approach improves the computational efficiency of FDTD calculations of diffraction coefficients by one to two orders of magnitude (16 : 1 demonstrated in 2-D; 64 : 1 or more projected for three-dimentions).

*Index Terms*—Diffraction, electromagnetic modeling of scatterers, finite-difference time-domain (FDTD), perfectly matched layer (PML).

## I. INTRODUCTION

**T**HE total-field/scattered-field (TF/SF) formulation [1] has been used extensively to model infinite plane wave excitation in two-dimensional (2-D) and three-dimensional (3-D) finite-difference time-domain (FDTD) grids. In this formulation, the plane wave excitation and the scatterer are confined within the so-called TF/SF boundary. The entire FDTD grid is enclosed within an absorbing boundary region (ABC), which terminates the grid. The perfectly matched layer (PML) absorbing region [2] has been used extensively to terminate FDTD grids. In this paper, we propose a *generalized total-field/scattered-field* (G-TF/SF) formulation to model infinite plane waves inside the FDTD computational space and in the PML absorbing boundary region. The proposed formulation allows plane waves to be terminated inside the PML absorbing boundary region. Correspondingly, the formulation allows plane waves to originate from within the PML absorbing boundary region. This is achieved by modeling the G-TF/SF boundary at required points inside the PML absorbing region.

An important application of this technique is that a scatterer illuminated by an infinite plane wave can be terminated inside

the PML absorbing region of the FDTD grid. Thus, the G-TF/SF formulation can be used to efficiently model infinite scatterers illuminated by plane waves in a relatively small grid. Previously proposed FDTD-based methods rely completely on the conventional TF/SF formulation and a *time-gating* procedure [3] to model infinite scatterers illuminated by plane waves within a finite FDTD grid. However, depending on the source angle and the observation points, this approach may require the use of a very large scatterer in the FDTD grid in order to permit time-gating. The G-TF/SF formulation proposed in this paper does not rely on time-gating to model infinite scatterers and hence, could be applied to efficiently model infinite 3-D scatterers in a compact FDTD grid.

In this paper, we develop the equations required to model the G-TF/SF boundary for a 2-D tranverse-magnetic (TM) FDTD grid. Then for purposes of demonstration, we apply this method to a specific total-field/scattered-field boundary configuration. Subsequently, we present numerical results of the incident plane wave generated inside the total-field region for various wave illumination angles when there is no scatterer in the FDTD grid. We compare these numerical results with the results obtained by using the conventional TF/SF formulation and observe an excellent agreement. Finally, we apply the G-TF/SF formulation to model 2-D TM diffraction of an infinite 45°-angle perfect-electrical-conductor (PEC) wedge and an infinite right-angle dielectric wedge. There is a very good correspondence between our numerical results of diffraction coefficients and well-known asymptotic results [4], [5] for the infinite 45°-PEC wedge. Numerical results of diffraction for the infinite dielectric wedge clearly show the advantage of using the G-TF/SF formulation over the conventional TF/SF formulation. It is expected that this method can be directly extended to 2-D transverse electric (TE) and 3-D FDTD grids.

## II. GENERAL DESCRIPTION OF THE METHOD

In this section, we propose the G-TF/SF formulation to model plane waves traveling into, or originating from, the PML absorbing boundary region in a 2-D TM FDTD grid. As in the conventional TF/SF formulation [1], the G-TF/SF formulation allows us to source an infinite plane wave by introducing an incident field at the G-TF/SF boundary. Consider an example of the G-TF/SF boundary configuration as shown in Fig. 1. Fig. 2 shows $\vec{E}$ and $\vec{H}$ fields in the vicinity of the G-TF/SF boundary. The shaded region in Figs. 1 and 2 shows the PML absorbing
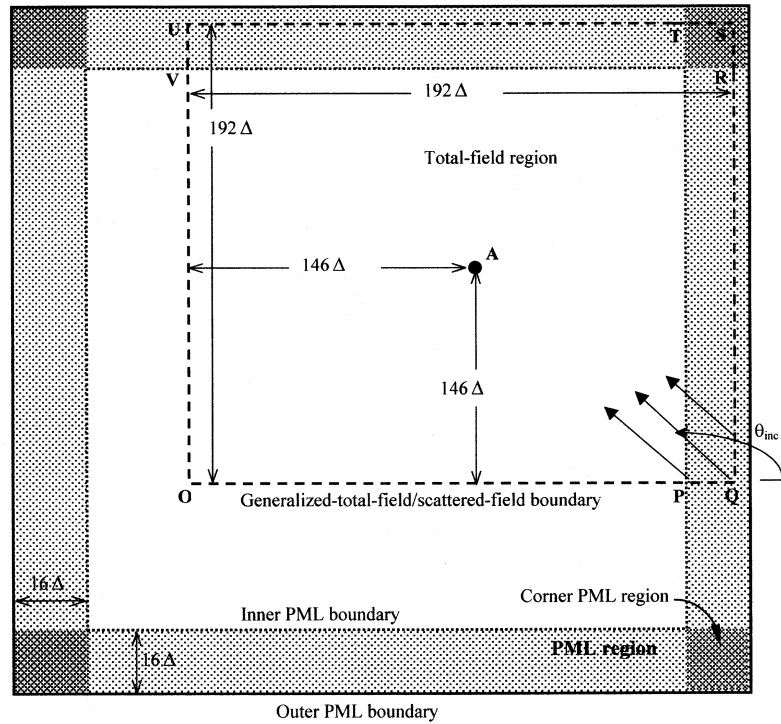
Fig. 1.   Example of a G-TF/SF boundary configuration in a 2-D TM FDTD grid. This figure shows a generic scatterer modeled in the grid. Observation point A is in the center of the total-field region. This figure is not drawn to scale.

boundary. Note that the back and right faces of the G-TF/SF boundary lie completely in the PML region. Also, some segments of the left and front G-TF/SF faces lie in the PML region. We state that the G-TF/SF boundary is generalized in the sense that it lies within both the free space part of the FDTD grid and the PML absorbing boundary region.

The field points shown in Fig. 2 in the PML absorbing region are the split fields ($H_x, H_y, E_{zx}$, and $E_{zy}$) arising in the 2-D TM Berenger PML formulation [2]. The split field pair, $E_{zx}(i,j)$ and $E_{zy}(i,j)$ lie at the same physical location in the FDTD grid as the $E_z(i,j)$ field. The total $E_z$ field in the PML region is the sum of the split fields ($E_{zx} + E_{zy}$).

The G-TF/SF boundary divides the computation grid into two regions *viz.*—the region (on and) inside the G-TF/SF boundary, which contains the total field (incident field and the scattered field); and the region outside the G-TF/SF boundary, which contains the scattered field only. For the 2-D TM FDTD grid, the G-TF/SF boundary lies along electric field points. The scatterers are modeled inside the total-field region i.e., within the G-TF/SF boundary. Also, the electric and magnetic field points on or inside the G-TF/SF boundary are total fields, while the fields outside this boundary are scattered fields. Thus, the (total) electric field points that lie on the G-TF/SF boundary and the scattered magnetic field points that are adjacent to the G-TF/SF boundary (Fig. 2) require special update equations. The segments of the G-TF/SF boundary that lie in free space are treated exactly like the conventional TF/SF boundary. Thus, for the special $E_z$, $H_x$, and $H_y$ points that lie in free space, we use the well-known special update equations for the conventional TF/SF boundary [1]. In the following sections, we derive the special update equations for the $H_x$, $H_y$, $E_{zx}$, and $E_{zy}$ fields
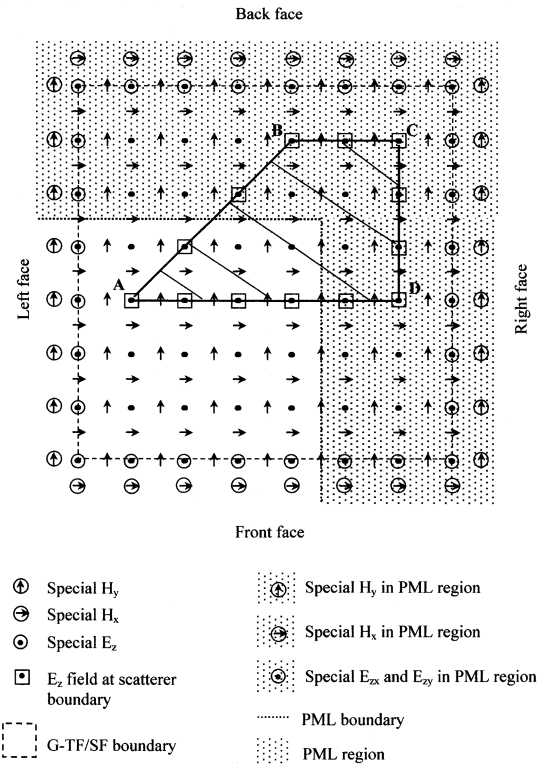


Fig. 2.   Electric and magnetic fields in a 2-D TM FDTD grid, where an infinite 45°-angle PEC wedge is modeled within the G-TF/SF boundary. The G-TF/SF boundary, scatterer boundary, and the special electric and magnetic field points are shown.

in the PML absorbing region and describe the method to implement these equations.

The G-TF/SF formulation described in this paper applies not only to the boundary configuration shown in Fig. 1, but also to any possible G-TF/SF boundary configuration in the FDTD grid. Also, the G-TF/SF formulation can be easily extended to the 2-D-TE FDTD grid and to the general 3-D FDTD grid.

## III. SPECIAL UPDATE EQUATIONS FOR G-TF/SF BOUNDARY IN PML REGION

In order to obtain the special update equations describing the G-TF/SF boundary in the PML absorbing region, we first review the usual update equations for the four 2-D TM fields in the PML absorbing region. These update equations are given by

$$
\begin{aligned}
H_x|_{i,j}^{n+1/2} = {} & D_{ax}^{\mathrm{PML}} H_x|_{i,j}^{n-1/2} \\
& + D_{bx}^{\mathrm{PML}}\bigg[\left(E_{zx}|_{i,j-1/2}^{n} + E_{zy}|_{i,j-1/2}^{n}\right) \\
& \qquad - \left(E_{zx}|_{i,j+1/2}^{n} + E_{zy}|_{i,j+1/2}^{n}\right)\bigg]
\end{aligned}
$$
(1a)

$$
\begin{aligned}
H_y|_{i,j}^{n+1/2} = {} & D_{ay}^{\mathrm{PML}} H_y|_{i,j}^{n-1/2} \\
& + D_{by}^{\mathrm{PML}}\bigg[\left(E_{zx}|_{i+1/2,j}^{n} + E_{zy}|_{i+1/2,j}^{n}\right) \\
& \qquad - \left(E_{zx}|_{i-1/2,j}^{n} + E_{zy}|_{i-1/2,j}^{n}\right)\bigg]
\end{aligned}
$$
(1b)

$$
\begin{aligned}
E_{zx}|_{i,j}^{n+1} = {} & C_{ax}^{\mathrm{PML}} E_{zx}|_{i,j}^{n} \\
& + C_{bx}^{\mathrm{PML}}\left[H_y|_{i+1/2,j}^{n+1/2} - H_y|_{i-1/2,j}^{n+1/2}\right]
\end{aligned}
$$
(1c)

$$
\begin{aligned}
E_{zy}|_{i,j}^{n+1} = {} & C_{ay}^{\mathrm{PML}} E_{zy}|_{i,j}^{n} \\
& + C_{by}^{\mathrm{PML}}\left[H_x|_{i,j-1/2}^{n+1/2} - H_x|_{i,j+1/2}^{n+1/2}\right].
\end{aligned}
$$
(1d)

Here the electric and magnetic field components $u|_{i,j}^{n} = u(i\Delta x, j\Delta y, n\Delta t)$. $i$, $j$, $n$ are integers. $(i\Delta x, j\Delta y)$ represents a space point in the uniform rectangular lattice (FDTD grid) with space increments $\Delta x$ and $\Delta y$ in the $x$ and $y$ directions. $n\Delta t$ is the time of observation and $\Delta t$ is the time increment. The medium-related constants are given by

$$
D_{ax}^{\mathrm{PML}}\left(\mu_{i,j}, \sigma_y^*(i,j)\right) = \frac{\left(1 - \frac{\sigma_y^*(i,j)\Delta t}{2\mu_{i,j}}\right)}{\left(1 + \frac{\sigma_y^*(i\cdot j)\Delta t}{2\mu_{i,j}}\right)}
$$
(2a)

$$
D_{bx}^{\mathrm{PML}}\left(\mu_{i,j}, \sigma_y^*(i,j)\right) = \frac{\left(\frac{\Delta t}{\mu_{i,j}\Delta x}\right)}{\left(1 + \frac{\sigma_y^*(i\cdot j)\Delta t}{2\mu_{i,j}}\right)}
$$
(2b)

$$
C_{ax}^{\mathrm{PML}}\left(\varepsilon_{i,j}, \sigma_x(i,j)\right) = \frac{\left(1 - \frac{\sigma_x(i,j)\Delta t}{2\varepsilon_{i,j}}\right)}{\left(1 + \frac{\sigma_x(i\cdot j)\Delta t}{2\varepsilon_{i,j}}\right)}
$$
(2c)

$$
C_{bx}^{\mathrm{PML}}\left(\varepsilon_{i,j}, \sigma_x(i,j)\right) = \frac{\left(\frac{\Delta t}{\varepsilon_{i,j}\Delta x}\right)}{\left(1 + \frac{\sigma_x(i\cdot j)\Delta t}{2\varepsilon_{i,j}}\right)}
$$
(2d)

Here, $\varepsilon$ is the electric permittivity in farads/meter, $\mu$ is the magnetic permeability in henrys/meter, $\sigma$ is the electric conductivity in siemens/meter and $\sigma^*$ is the equivalent magnetic loss in ohms/meter. $D_{ay}^{\mathrm{PML}}$, $D_{by}^{\mathrm{PML}}$, $C_{ay}^{\mathrm{PML}}$, and $C_{by}^{\mathrm{PML}}$ are obtained by replacing $x$ by $y$ and $y$ by $x$ in (2a)–(2d).

Consider the (total) electric field points $(E_{zx}, E_{zy})$ on the front or back G-TF/SF face boundary inside the PML region. Since the PML update equation of $E_{zy}$ (1d) involves total and scattered $H_x$ fields on either side of the boundary, (1d) is invalid and we require special update equations for $E_{zy}$. Correspondingly, for electric field points on the left and right G-TF/SF boundary inside the PML region, (1c) is invalid and we require special update equations for $E_{zx}$. Following the procedure described in [6] and adding the appropriate incident $H_x$ or $H_y$ fields to (1d) and (1c), we get

Front G-TF/SF face in PML :
$$
E_{zy,\mathrm{tot}}|_{i,j}^{n+1} = \left[E_{zy,\mathrm{tot}}|_{i,j}^{n+1}\right]_{\mathrm{PML}} + C_{by}^{\mathrm{PML}} H_{x,\mathrm{inc}}|_{i,j-1/2}^{n+1/2}
$$
(3a)

Back G-TF/SFface in PML :
$$
E_{zy,\mathrm{tot}}|_{i,j}^{n+1} = \left[E_{zy,\mathrm{tot}}|_{i,j}^{n+1}\right]_{\mathrm{PML}} - C_{by}^{\mathrm{PML}} H_{x,\mathrm{inc}}|_{i,j+1/2}^{n+1/2}
$$
(3b)

Left G-TF/SFface in PML :
$$
E_{zx,\mathrm{tot}}|_{i,j}^{n+1} = \left[E_{zx,\mathrm{tot}}|_{i,j}^{n+1}\right]_{\mathrm{PML}} - C_{bx}^{\mathrm{PML}} H_{y,\mathrm{inc}}|_{i-1/2,j}^{n+1/2}
$$
(3c)

Right G-TF/SFface in PML :
$$
E_{zx,\mathrm{tot}}|_{i,j}^{n+1} = \left[E_{zx,\mathrm{tot}}|_{i,j}^{n+1}\right]_{PML} + C_{bx}^{\mathrm{PML}} H_{y,\mathrm{inc}}|_{i+1/2,j}^{n+1/2}
$$
(3d)

where $\left[E_{zy,\mathrm{tot}}|_{i,j}^{n+1}\right]_{\mathrm{PML}}$ and $\left[E_{zx,\mathrm{tot}}|_{i,j}^{n+1}\right]_{\mathrm{PML}}$ are the updated fields obtained using (1d) and (1c), respectively.

Consider the (scattered) $H_x$ field points adjacent to the front or back G-TF/SF boundary in the PML region. Since the PML update equation for $H_x$ (1a) involves total and scattered ($E_{zx} + E_{zy}$) fields, (1a) is invalid and we require special update equations for $H_x$. Correspondingly, the $H_y$ field points adjacent to the left and right G-TF/SF boundary in the PML region require special update equations since (1b) is invalid. Following the procedure described in [6] and adding the appropriate incident ($E_{zx} + E_{zy}$) field to (1a) and (1b), we get

Front G-TF/SF face in PML :
$$
\begin{aligned}
H_{x,\mathrm{scat}}|_{i,j}^{n+1/2} = {} & \left[H_{x,\mathrm{scat}}|_{i,j}^{n+1/2}\right]_{\mathrm{PML}} \\
& + D_{bx}^{\mathrm{PML}}\left(E_{zx,\mathrm{inc}}|_{i,j+1/2}^{n} + E_{zy,\mathrm{inc}}|_{i,j+1/2}^{n}\right)
\end{aligned}
$$
(4a)

Back G-TF/SFface in PML :
$$
\begin{aligned}
H_{x,\mathrm{scat}}|_{i,j}^{n+1/2} = {} & \left[H_{x,\mathrm{scat}}|_{i,j}^{n+1/2}\right]_{\mathrm{PML}} \\
& - D_{bx}^{\mathrm{PML}}\left(E_{zx,\mathrm{inc}}|_{i,j-1/2}^{n} + E_{zy,\mathrm{inc}}|_{i,j-1/2}^{n}\right)
\end{aligned}
$$
(4b)

Left TF/SF face in PML :
$$
\begin{aligned}
H_{y,\mathrm{scat}}|_{i,j}^{n+1/2} = {} & \left[H_{y,\mathrm{scat}}|_{i,j}^{n+1/2}\right]_{\mathrm{PML}} \\
& - D_{by}^{\mathrm{PML}}\left(E_{zx,\mathrm{inc}}|_{i+1/2,j}^{n} + E_{zy,\mathrm{inc}}|_{i+1/2,j}^{n}\right)
\end{aligned}
$$
(4c)

Right TF/SF face in PML :

$$H_{y,\text{scat}}|_{i,j}^{n+1/2} = \left[ H_{y,\text{scat}}|_{i,j}^{n+1/2} \right]_{\text{PML}}$$
$$+ D_{by}^{\text{PML}} \left( E_{zx,\text{inc}}|_{i-1/2,j}^{n} + E_{zy,\text{inc}}|_{i-1/2,j}^{n} \right)$$

$$(4d)$$

where $\left[ H_{x,\text{scat}}|_{i,j}^{n+1/2} \right]_{PML}$ and $\left[ H_{y,\text{scat}}|_{i,j}^{n+1/2} \right]_{PML}$ are the updated fields obtained using (1a) and (1b), respectively.

Thus, (3a)–(3d), (4a)–(4d), and the special update equations of the conventional TF/SF formulation in free space [1] represent the complete set of special electric and magnetic-field update equations required to model the G-TF/SF boundary for any 2-D TM grid. Equations (3a)–(3d) and (4a)–(4d) can be easily implemented as long as we have knowledge of the appropriate incident fields in the PML region. Note that in these equations, knowledge of the total incident electric field ($E_{zx} + E_{zy}$) is required, and not the individual split incident fields.

## IV. INCIDENT FIELDS FOR G-TF/SF BOUNDARY INSIDE PML REGION

In this section, we describe our proposed method to obtain the incident magnetic and electric fields in the PML region that are required in (3a)–(3d) and (4a)–(4d). The incident fields required in the (free space) special update equations for the TF/SF boundary are readily obtained using a table look-up procedure described in [6].

According to Berenger's PML theory, if the electric loss constants ($\sigma_x$ or $\sigma_y$) and magnetic loss constants ($\sigma_x^*$ or $\sigma_y^*$) in the PML region are chosen appropriately, the various $\vec{E}$ and $\vec{H}$ field components, $\psi$, propagate within the PML region according to

$$\psi = \psi_0 e^{j\omega(t - (x\cos\phi + y\sin\phi)/c)}$$
$$\cdot e^{-(\sigma_x \cos\phi)/(\varepsilon_0 c)x} e^{-(\sigma_y \sin\phi)/(\varepsilon_0 c)y}. \quad (5)$$

Here $\psi_0$ is the field component at a given reference point and $\phi$ is the wave propagation angle with respect to the $y$ axis. $\omega$ is the angular frequency, $t$ is the time and $c$ is the speed of light. It is well known that the wave in the PML region propagates normally to the electric field with the speed of light in vacuum and undergoes an exponential decay with PML depth.

We could directly use (5) to obtain the incident $\vec{E}$ and $\vec{H}$ field components required in (3a)–(3d) and (4a)–(4d) in the PML region. However, we have determined that the amplitude of the plane wave does not attenuate exactly as predicted by (5). If (5) is used to obtain the required incident $\vec{E}$ and $\vec{H}$ field components, unacceptable numerical errors occur. Thus, we propose an alternate numerical method to accurately determine the incident $\vec{E}$ and $\vec{H}$ fields within the PML.

We assume the basic form of (5) to be valid. However we do not assume a perfectly exponential decay factor for the amplitude of the plane wave in the PML region. Rewriting (5) for the 2-D FDTD grid, by retaining its basic form, we get

$$\psi_{\text{inc}}^{\text{num}} = X_0^{\text{num}} A_{\text{PML}} (\theta_{\text{inc}}, \xi_x, \xi_y). \quad (6)$$

Here, $\psi_{\text{inc}}^{\text{num}}$ represents the required incident $\vec{E}$ or $\vec{H}$ field component in the PML region. $X_0^{\text{num}}$ is the corresponding free space incident field, which can be numerically obtained using the table look-up procedure of [6]. $A_{\text{PML}}(\theta_{\text{inc}}, \xi_x, \xi_y)$ is the appropriate multiplying factor at the observation point in the PML region, where: $\theta_{\text{inc}}$ is the incident angle of the plane wave; $\xi_x = d_x\zeta_{x,\text{PML}}$; $\xi_y = d_y\zeta_{y,\text{PML}}$; $\zeta_{x,\text{PML}}$ and $\zeta_{y,\text{PML}}$ are the electric or magnetic loss constants at the observation point in the PML region in the $x$ and $y$ directions, respectively; and $d_x$ and $d_y$ are the depths of the observation point inside the PML region in the $x$ and $y$ directions, respectively.

In the 2-D FDTD grid, we assign losses to the different PML regions as proposed by Berenger [2] and [7]. For the noncorner front and back PML regions, $\zeta_{x,\text{PML}} = 0$; and for the noncorner left and right PML regions, $\zeta_{y,\text{PML}} = 0$. For the corner regions, both $\zeta_{x,\text{PML}}$ and $\zeta_{y,\text{PML}}$ are nonzero. Thus, the problem of obtaining $A_{\text{PML}}(\theta_{\text{inc}}, \xi_x, \xi_y)$ at all the desired points in the PML region reduces to: see (7) at the bottom of the page, where $A_{x,\text{PML}} = A_{\text{PML}}(\theta_{\text{inc}}, \xi_x, 0)$ and $A_{y,\text{PML}} = A_{\text{PML}}(\theta_{\text{inc}}, 0, \xi_y)$.

We now summarize the numerical method used to obtain $A_{x,\text{PML}}$ and $A_{y,\text{PML}}$ for a given FDTD grid configuration and an arbitrary $\theta_{\text{inc}}$. Our method is to use preliminary FDTD runs to calibrate the performance of the PML region. In the preliminary FDTD runs, we illuminate the desired PML region (front, back, left, or right) of the grid with a pulsed incident plane wave having a center frequency, $f_o$ and a full-width at half-maximum (FWHM) bandwidth, $\Delta f$. We record the amplitude of the electric field ($E_{zx} + E_{zy}$) and magnetic fields ($H_x$ or $H_y$). Let $F_{o,\text{inc}}^{\text{PML}}(\theta_{\text{inc}}, d)$ denote any one of these three field amplitudes at each desired depth, $d$, in the PML region. We also compute the amplitude of the corresponding incident, electric, and magnetic fields, $F_{o,\text{inc}}^{\text{freespace}}(\theta_{\text{inc}}, d)$, in free space. Then, for a wave impinging upon a given PML region, we obtain the attenuation factor, $\text{attn}_{\text{PML}}(\theta_{\text{inc}}, d)$, as

$$\text{attn}_{\text{PML}}(\theta_{\text{inc}}, d) = \frac{F_{o,\text{inc}}^{\text{PML}}(\theta_{\text{inc}}, d)}{F_{o,\text{inc}}^{\text{freespace}}(\theta_{\text{inc}}, d)}. \quad (8a)$$

Similarly, for a wave originating within a given PML region, we obtain the amplification factor, $\text{Ampf}_{\text{PML}}(\theta_{\text{inc}}, d)$, as

$$\text{Ampf}_{\text{PML}}(\theta_{inc}, d) = \frac{F_{o,\text{inc}}^{\text{freespace}}(\pi + \theta_{inc}, d)}{F_{o,\text{inc}}^{\text{PML}}(\pi + \theta_{\text{inc}}, d)}. \quad (8b)$$

$$A_{\text{PML}}(\theta_{\text{inc}}, \xi_x, \xi_y) = \begin{cases} A_{x,\text{PML}}, & \text{for noncorner left/right PML regions} \\ A_{y,\text{PML}}, & \text{for noncorner front/back PML regions} \\ A_{x,\text{PML}} A_{y,\text{PML}}, & \text{for corner PML regions} \end{cases} \quad (7)$$

Note that $\mathrm{Ampf}_{\mathrm{PML}}(\theta_{\mathrm{inc}})$ is obtained in the preliminary FDTD run by illuminating the given PML region with a plane wave incident at $\theta_{\mathrm{inc}} + 180°$.

For a given angle of incidence, we determine if each G-TF/SF boundary segment lies in a PML boundary region that sources or terminates the incident plane waves. A given PML boundary region (left, right, back, or front) is considered as a *PML-wave-sourcing-boundary* if the initial plane wave source point is in this PML boundary region. In all other cases, the PML boundary region is considered as a *PML-wave terminating-boundary*. By using this definition, if the wave source point is in a corner PML region, then both the PML regions that form the corner are considered as *PML-wave-sourcing-boundary* regions.

Let $A_{w,\mathrm{PML}}$ represent either $A_{x,\mathrm{PML}}$ or $A_{y,\mathrm{PML}}$. Then, for G-TF/SF boundary points in noncorner and corner PML regions, we obtain $A_{w,\mathrm{PML}}$ by using

G-TF/SF boundarypoint in

      PML-wave-terminating-boundary:

$$A_{w,\mathrm{PML}} = \mathrm{attn}_{w,\mathrm{PML}} \qquad (9a)$$

G-TF/SF boundary point in

      PML-wave-sourcing-boundary:

$$A_{w,\mathrm{PML}} = \mathrm{Ampf}_{w,\mathrm{PML}} \qquad (9b)$$

Thus, at the G-TF/SF boundary points that terminate the incident plane wave in noncorner PML regions, the incident wave is attenuated by the factor $\mathrm{Attn}_{w,\mathrm{PML}}$. Correspondingly, at the G-TF/SF boundary points that source the incident plane wave in noncorner PML regions, the incident wave is amplified by the factor $\mathrm{Ampf}_{w,\mathrm{PML}}$. At G-TF/SF boundary points that lie in any one of the corner PML regions, $A_{\mathrm{PML}}$ in (7) is thus the product of the attenuation ($\mathrm{Attn}_{w,\mathrm{PML}}$) or amplification ($\mathrm{Ampf}_{w,\mathrm{PML}}$) factors of the two PML regions that form the corner (e.g., back-right corner).

Using (7)– (9), we numerically obtain $A_{\mathrm{PML}}$ at all desired G-TF/SF boundary points in the PML region for the appropriate $\vec{E}$ and $\vec{H}$ field components. We then use (6) to obtain the incident $\vec{E}$ and $\vec{H}$ field components at any point in the PML region. The incident $\vec{E}$ and $\vec{H}$ fields are then used in the G-TF/SF special update equations, (3a)–(3d) and (4a)–(4d), respectively. We note that $A_{\mathrm{PML}}$ is independent of the scatterer being modeled within the G-TF/SF boundary used in the preliminary runs. Thus, a lookup table of $A_{\mathrm{PML}}(\theta_{\mathrm{inc}}, \xi_x, \xi_y)$ can be easily obtained for a given FDTD grid discretization, a given source frequency spectrum and a given PML loss gradient. Such a lookup table can be used to efficiently model infinite scatterers illuminated by an incident plane wave.

Techniques such as the near-field-to-far-field transformation [8] require the knowledge of all field variables on a parallelepiped in the scattered-field region. When the G-TF/SF formulation is used, this implies that we require the (free space) scattered fields within the PML absorbing region. We can obtain these scattered fields within the PML absorbing region by using the attenuation factors (8) that arise in our preliminary calibration runs. Thus, we can apply techniques such as near-field-to-far-field transformations in conjunction with the G-TF/SF formulation.

## V. BASIC EXAMPLE: G-TF/SF BOUNDARY CONFIGURATION WITH NO SCATTERER

### A. Problem Setup

In this section, we present numerical results of the incident plane wave for various angles of incidence obtained using the G-TF/SF formulation for the geometry shown in Fig. 1 with no scatterer. The FDTD grid has square cells of side length $\Delta = \lambda_o/20$, where $\lambda_o$ is the wavelength corresponding to the center frequency of the source, $f_o$ (850 MHz). The G-TF/SF boundary shown in Fig. 1 has a side length (OQ) of $192\Delta$. The PML absorbing boundary region terminating the FDTD grid is $16\Delta$ deep. The segments of the left and right G-TF/SF boundary, UV and PQ, respectively, that extend into the PML absorbing boundary region are $12\Delta$ in length. We model the PML region [4], [5] such that the loss within the region increases with PML depth, $d$, as

$$\sigma(d) = \sigma_{\max} \left( \frac{d}{\delta_{\mathrm{PML}}} \right)^n. \qquad (10)$$

Here $n$ is a user defined constant and $\delta_{\mathrm{PML}}$ is the total PML thickness. $\sigma_{\max}$ is given by

$$\sigma_{\max} = -\frac{\log(R_0)(n+1)\varepsilon_0 c}{2\delta_{\mathrm{PML}}} \qquad (11)$$

where $R_o$ is the reflection coefficient at normal incidence for PML boundary that is specified by the user. In order to achieve accurate results, we choose $R_o$ to be $10^{-16}$ and we use a quadratically graded PML loss, $n = 2$.

### B. Preliminary PML Calibration Runs

In order to obtain $A_{\mathrm{PML}}(\theta_{\mathrm{inc}}, \xi_x, \xi_y)$ for a given incident angle and all PML depths, we set up two preliminary FDTD runs in which plane waves propagate into the PML regions of interest. Fig. 3(a) and (b) illustrate, respectively, the geometry used to obtain $A_{\mathrm{PML}}(\theta_{\mathrm{inc}}, \xi_x, \xi_y)$ in the back PML region and the right PML region. In both preliminary FDTD runs, we use a gaussian modulated sinusoidal source with $f_o = 850$ MHz and $\Delta f = 600$ MHz. The FDTD grid has square cells of side length $\Delta = \lambda_o/20$, where $\lambda_o$ is the wavelength corresponding to the center frequency of the source, $f_o$ (850 MHz). As shown in Fig. 3, in the preliminary FDTD runs we generate a plane wave in the PML region of interest by using a TF/SF boundary with only one side. For example, to obtain a plane wave propagating into the back PML region [Fig. 3(a)], we use a TF/SF boundary with only the front side. Far away from the edges of the front side TF/SF boundary, this gives a plane wave in the back PML region of interest. Thus, we measure the amplitude of the plane wave at points along line AB [Fig. 3(a)] in the PML region of interest. In one preliminary run, we obtain $\mathrm{attn}_{y,\mathrm{PML}}$ and $\mathrm{Ampf}_{y,\mathrm{PML}}$ for all PML depths ($d_y$) in the back PML region by illuminating this region and using (8a)–(8b). Correspondingly, in another preliminary run [Fig. 3(b)] we obtain $\mathrm{attn}_{x,\mathrm{PML}}$ and $\mathrm{Ampf}_{x,\mathrm{PML}}$ for all PML depths ($d_x$) in the right PML region by illuminating this region and using (8a)–(8b).

We now obtain $A_{\mathrm{PML}}$ from $\mathrm{attn}_{x,\mathrm{PML}}$, $\mathrm{Ampf}_{x,\mathrm{PML}}$, $\mathrm{attn}_{y,\mathrm{PML}}$, and $\mathrm{Ampf}_{y,\mathrm{PML}}$ for all G-TF/SF boundary seg-
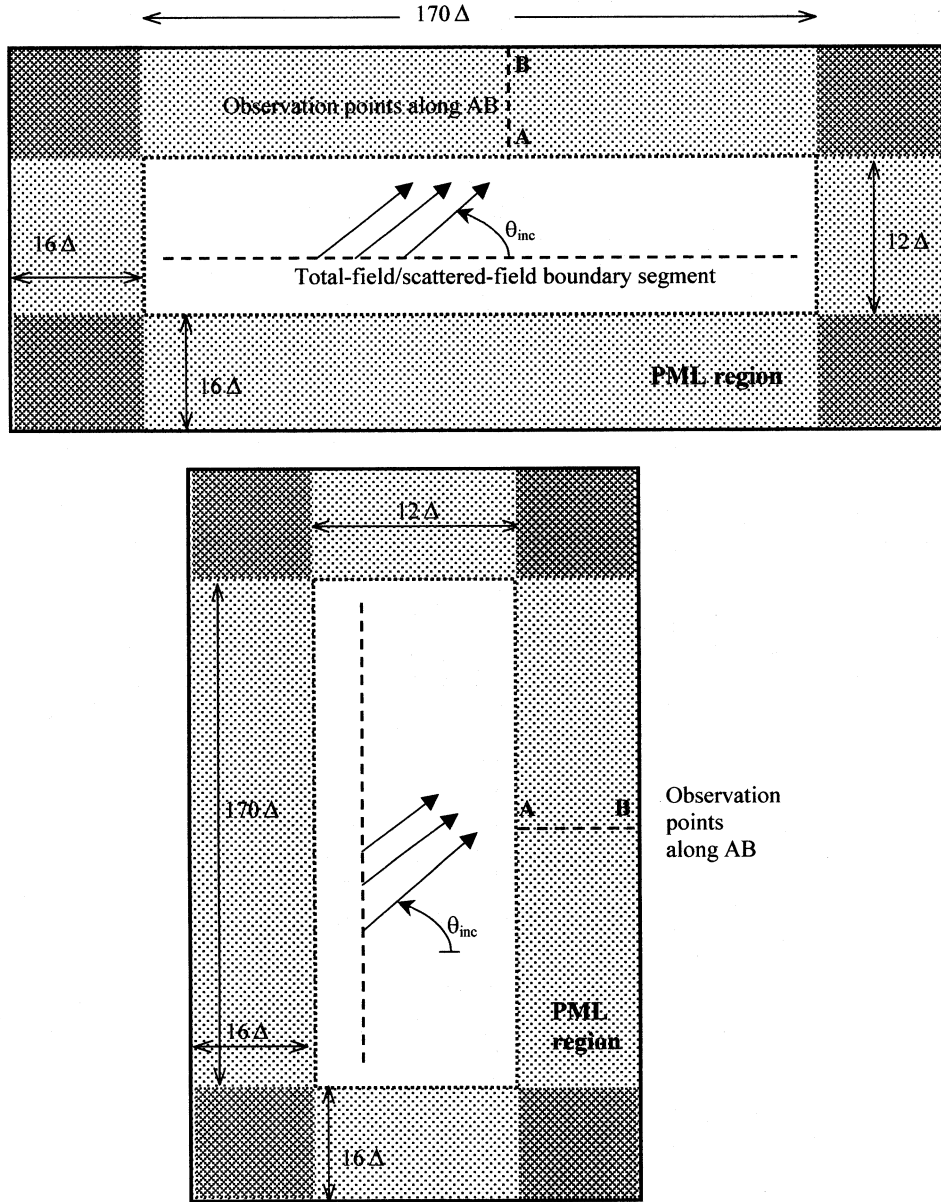
Fig. 3. Geometry of preliminary PML calibration runs used to measure attenuation of plane waves in (a) the back PML region and (b) in the right PML region. Observation points in the PML region are chosen along the line AB.

ments in PML and all angles of incidence, by identifying the *PML-wave-terminating* and *PML-wave-sourcing* boundary regions and using (7) and (9), as

*Left G-TF/SF boundary in PML region* (VU in Fig. 1):

$$A_{\mathrm{PML}} = A_{y,\mathrm{PML}}(y)$$
$$= \begin{cases} \mathrm{attn}_{y,\mathrm{PML}}(y), & 0° < \theta_{inc} \le 270° \\ \mathrm{Ampf}_{y,\mathrm{PML}}(y) & 270° < \theta_{\mathrm{inc}} \le 360° \end{cases}$$

$$(12a)$$

where $0 \le y \le \mathrm{distance(VU)}$.

*Back G-TF/SF boundary in noncorner PML region* (UT in Fig. 1):

$$A_{\mathrm{PML}} = A_{y,\mathrm{PML}}(y_o)$$

$$= \begin{cases} \mathrm{attn}_{y,\mathrm{PML}}(y_o), & 0° < \theta_{\mathrm{inc}} \le 180° \\ \mathrm{Ampf}_{y,\mathrm{PML}}(y_o), & 180° < \theta_{inc} \le 360° \end{cases}$$

$$(12b)$$

where $y_o = \mathrm{distance(VU)}$.

*Back G-TF/SF boundary in corner PML region* (TS in Fig. 1): see (12c) at the bottom of the next page where $y_o = \mathrm{distance}$ (VU) and $0 \le x \le \mathrm{distance}$ (TS).

*Front G-TF/SF boundary in PML region* (PQ in Fig. 1):

$$A_{\mathrm{PML}} = A_{x,\mathrm{PML}}(x)$$
$$= \begin{cases} \mathrm{attn}_{x,\mathrm{PML}}(x), & 0° < \theta_{\mathrm{inc}} \le 90° \\ \mathrm{Ampf}_{x,\mathrm{PML}}(x), & 90° < \theta_{\mathrm{inc}} \le 180° \\ \mathrm{attn}_{x,\mathrm{PML}}(x), & 180° < \theta_{\mathrm{inc}} \le 360° \end{cases}$$

$$(12d)$$

where $0 \le x \le \mathrm{distance(PQ)}$.

*Right G-TF/SF boundary in noncorner PML region* (QR in Fig. 1):

$$A_{\mathrm{PML}} = A_{x,\mathrm{PML}}(x_o)$$
$$= \begin{cases} \mathrm{attn}_{x,\mathrm{PML}}(x_o), & 0° < \theta_{\mathrm{inc}} \leq 90° \\ \mathrm{Ampf}_{x,\mathrm{PML}}(x_o), & 90° < \theta_{\mathrm{inc}} \leq 270° \\ \mathrm{attn}_{x,\mathrm{PML}}(x_o), & 270° < \theta_{\mathrm{inc}} \leq 360° \end{cases}$$

(12e)

where $x_o = \mathrm{distance}(PQ)$.

*Right G-TF/SF boundary in corner PML region* (RS in Fig. 1): see (12f) at the bottom of the page where $x_o = \mathrm{distance}(PQ)$ and $0 \leq y \leq \mathrm{distance}(RS)$.

We use (12a)–(12f) and (6) to obtain the incident $\vec{E}$ and $\vec{H}$ field components at any point in the PML region. We then use the special update equations, (3a)–(3d) and (4a)–(4d), to simulate the G-TF/SF boundary in the PML absorbing boundary region. Note that in the preliminary runs described here, the method used to obtain a plane wave in the PML region requires a larger FDTD grid than the actual problem of interest, because the plane wave is simulated only far away from the edge of the single TF/SF boundary. Even though this increases the computational overhead, this is only required initially in the preliminary runs.

### C. Numerical Results

We now show numerical results for the plane wave generated at several angles of incidence for the G-TF/SF boundary configuration shown in Fig. 1 with no scatterer. We show results for three incident plane wave source angles ($\theta_{\mathrm{inc}}$), *viz.*—when the initial plane wave source point is in free space ($\theta_{\mathrm{inc}} = 30°$), when the initial plane wave source point is in the noncorner PML region ($\theta_{\mathrm{inc}} = 120°$), and when the initial plane wave source point is in the corner PML region ($\theta_{\mathrm{inc}} = 210°$). As in the preliminary FDTD runs, we obtain the numerical results using a gaussian modulated sinusoid source with $f_o = 850\,\mathrm{MHz}$ and $\Delta f = 600\,\mathrm{MHz}$.

Figs. 4(a)–(c) show the snapshot of the numerical electric field in the entire 2-D-FDTD grid (excluding the PML absorbing region) at a given time (250 time steps) for incident source angles $\theta_{\mathrm{inc}} = 30°$, $\theta_{\mathrm{inc}} = 120°$, and $\theta_{\mathrm{inc}} = 210°$, respectively. These results show that the G-TF/SF boundary effectively generates an infinite wideband plane wave within the total-field region. This provides the validity of our method. Additionally, we

compare the accuracy of the numerical results of the G-TF/SF formulation to the conventional TF/SF formulation. In both numerical approaches, we use the same gaussian modulated source and the same TF/SF boundary dimensions with no scatterer. Fig. 5(a) compares the time variation of the electric field observed at the center of the total field region (point A), by using the G-TF/SF formulation and the conventional TF/SF formulation, for incident source angles $\theta_{\mathrm{inc}} = 30°$ and $\theta_{\mathrm{inc}} = 120°$. All four sets of data in this figure agree to four decimal places. Fig. 5(b) shows the corresponding data for $\theta_{\mathrm{inc}} = 210°$. Here the worst-case difference between the G-TF/SF and TF/SF results is 6%. Overall, there is a very good correspondence of the G-TF/SF computed incident fields with the conventional TF/SF results.

Several strategies can be employed to obtain more accurate results for the case when $180° < \theta_{\mathrm{inc}} \leq 270°$. For example, in this particular case, $A_{\mathrm{PML}}(\theta_{\mathrm{inc}}, \xi_x, \xi_y)$ in the corner PML region can be directly obtained from a preliminary calibration run by measuring $F_{o,\mathrm{inc}}^{\mathrm{PML}}(\theta_{\mathrm{inc}}, d)$ and using (8b). Since this would not involve a product of two independent numerical terms, as in (7), we expect the associated numerical error to be greatly reduced. We are investigating this and similar strategies in our ongoing work. Such strategies will be important when the method is extended to 3-D problems, since we expect the worst-case error to increase when the plane wave is generated from the corner PML region of the 3-D grid. We further note, that by using exponential time-stepping [9] in the PML instead of ordinary time-stepping, we do not get any improvement in the numerical results presented here.

## VI. SCATTERERS MODELED WITHIN THE G-TF/SF BOUNDARY

In this section, we show the method to efficiently model infinite scatterers by using the G-TF/SF formulation. Fig. 6 shows an infinite 45°-angle PEC wedge modeled within the G-TF/SF boundary. The scatterer is modeled in such a way that only the vertex of interest, A, lies in the free-space region of the grid. All the other vertices, B, C, and D, and wedge-sides, BC and CD, are modeled within the PML absorbing boundary region. The G-TF/SF boundary is used to illuminate the scatterer with an infinite plane wave. Since the nature of the PML region is to absorb all electromagnetic energy, we expect that any scattering due to wedge vertices and sides within the PML is attenuated. Thus, at observation points (such as E, F, and G) in the

$$A_{\mathrm{PML}} = A_{y,\mathrm{PML}}(y_o) A_{x,\mathrm{PML}}(x) = \begin{cases} \mathrm{attn}_{y,\mathrm{PML}}(y_o)\,\mathrm{attn}_{x,\mathrm{PML}}(x), & 0° < \theta_{\mathrm{inc}} \leq 180° \\ \mathrm{Ampf}_{y,\mathrm{PML}}(y_o)\,\mathrm{Ampf}_{x,\mathrm{PML}}(x), & 180° < \theta_{\mathrm{inc}} \leq 270° \\ \mathrm{Ampf}_{y,\mathrm{PML}}(y_o)\,\mathrm{attn}_{x,\mathrm{PML}}(x), & 270° < \theta_{\mathrm{inc}} \leq 360° \end{cases}$$

(12c)

$$A_{\mathrm{PML}} = A_{x,\mathrm{PML}}(x_o) A_{y,\mathrm{PML}}(y) = \begin{cases} \mathrm{attn}_{x,\mathrm{PML}}(x_o)\,\mathrm{attn}_{y,\mathrm{PML}}(y), & 0° < \theta_{\mathrm{inc}} \leq 90° \\ \mathrm{Ampf}_{x,\mathrm{PML}}(x_o)\,\mathrm{attn}_{y,\mathrm{PML}}(y), & 90° < \theta_{inc} \leq 180° \\ \mathrm{Ampf}_{x,\mathrm{PML}}(x_o)\,\mathrm{Ampf}_{y,\mathrm{PML}}(y), & 180° < \theta_{\mathrm{inc}} \leq 270° \\ \mathrm{attn}_{x,\mathrm{PML}}(x_o)\,\mathrm{attn}_{y,\mathrm{PML}}(y), & 270° < \theta_{\mathrm{inc}} \leq 360° \end{cases}$$
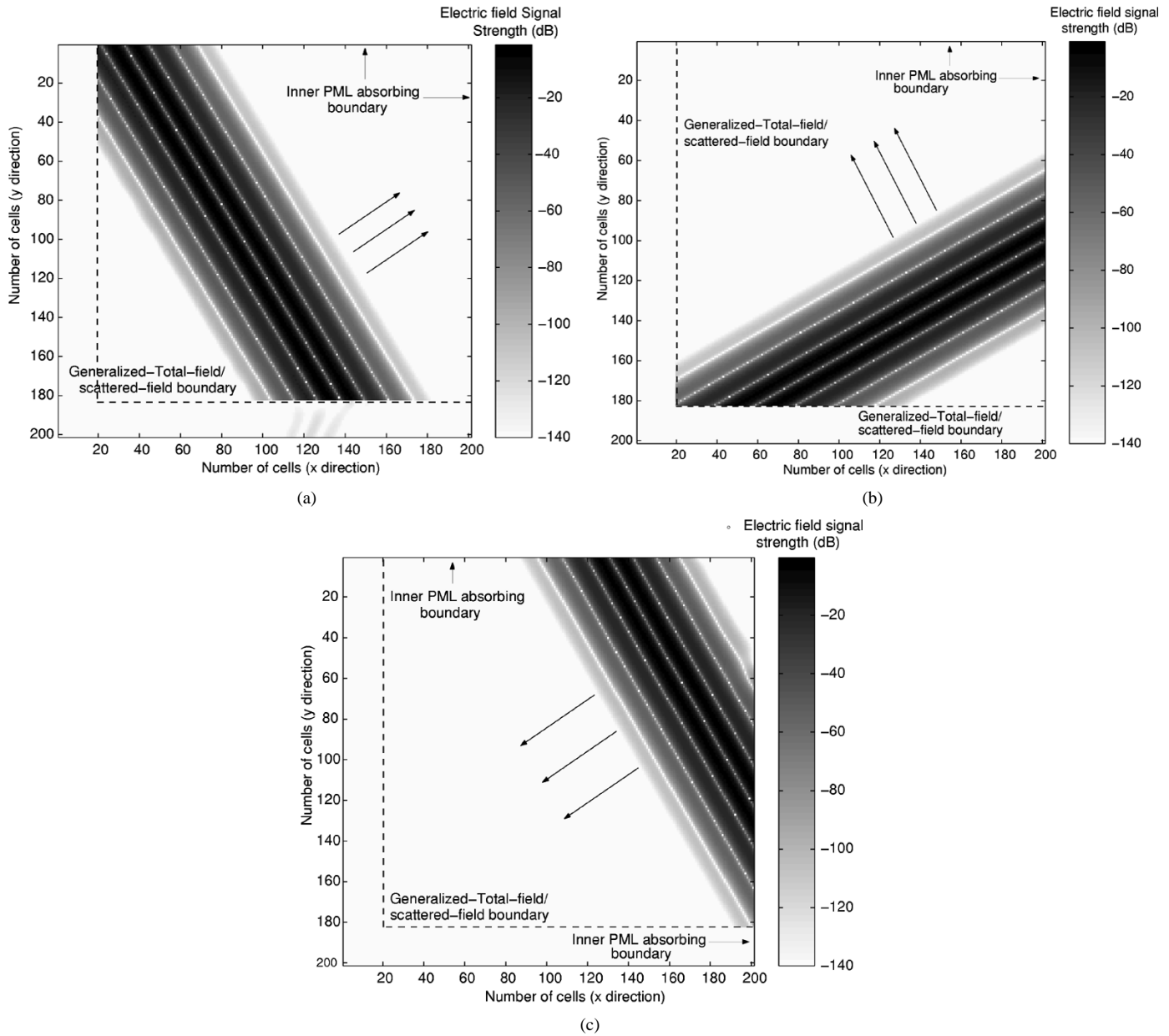
(12f)

Fig. 4.   Snapshot of the plane waves ($E_z$ field) generated using the G-TF/SF formulation in the 2-D TM FDTD grid of Fig. 1 with no scatterer at 250 time steps. Results are shown for incident source angle, (a) $\theta_{\mathrm{inc}} = 30°$, (b) $\theta_{\mathrm{inc}} = 120°$ and $\theta_{\mathrm{inc}} = 210°$. Waves are not shown inside the PML absorbing region.

free-space region of the FDTD grid, we observe scattering only from the wedge of interest, A. In this manner, we model an *infinite* scatterer within a compact FDTD grid.

In the following sections, we apply the G-TF/SF formulation to efficiently model 2-D TM diffraction of an infinite 45°-angle PEC wedge and an infinite right-angle dielectric wedge. We show that there is a very good correspondence between our numerical results and well-known asymptotic results [4], [5] for the infinite PEC wedge. Additionally, we present numerical results that clearly show the advantage of using the G-TF/SF formulation over the conventional TF/SF formulation to efficiently model infinite scatterers illuminated by plane waves.

### A. Numerical Results for an Infinite 45° PEC Wedge

In this section, we present numerical results for the 2-D TM diffraction coefficients of the infinite 45°-angle PEC wedge

modeled using the geometry shown in Fig. 6. This example represents the worst case wherein the scatterer penetrates the PML at the most oblique possible angle. In Fig. 6, the straight side (AD) of the 45°-angle wedge is modeled with a side length of $122\Delta$, while the oblique side (AB) of the wedge has a side length of $173\Delta$. The left (AB) and front (AD) sides of the scatterer extend into the PML absorbing region up to a PML depth of $42\Delta$. Thus, the back (BC) and right (CD) sides of the scatterer lie at a depth of $42\Delta$ inside the PML absorbing region. As shown in Fig. 2, the oblique 45°-angle scatterer boundary (AB) lies exactly along the $E_z$ (or $E_{zx} + E_{zy}$) field points, since we use a uniform orthogonal FDTD grid. The PML absorbing boundary region terminating the FDTD grid is chosen to be $48\Delta$ deep to provide a smaller loss gradation in the PML. This is required in order to mitigate diffraction from the point where the scatterer penetrates obliquely into the
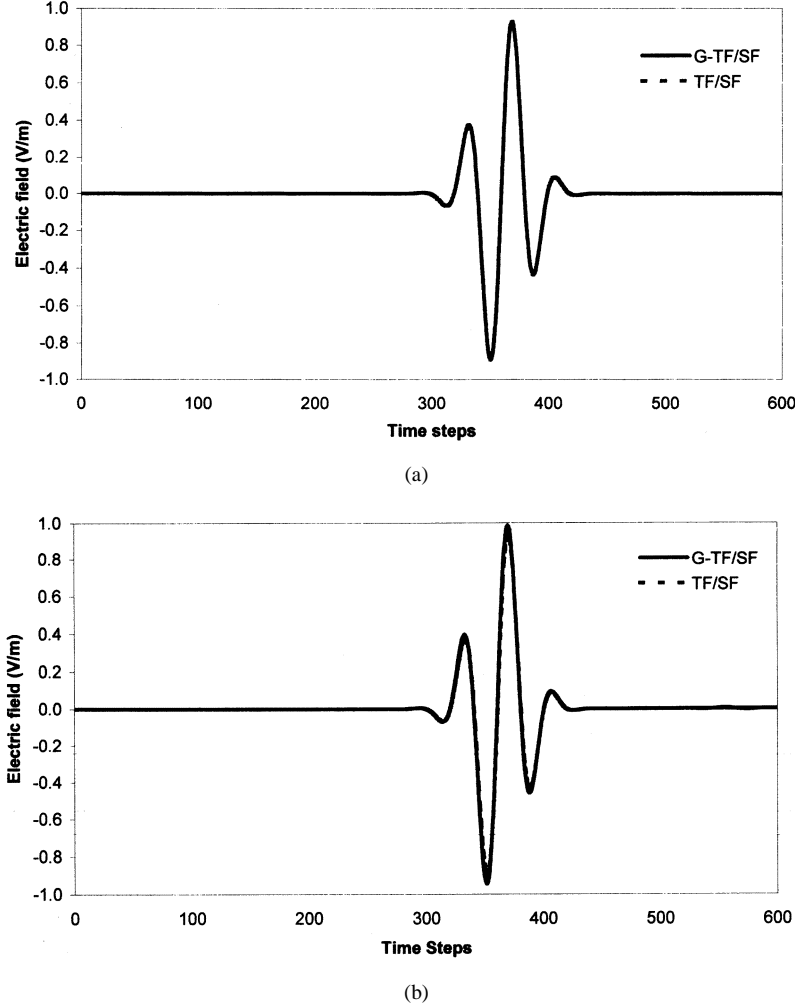
(a)



(b)

Fig. 5. Time variation of the incident $E_z$ field at the center of the total field region (point A) in the 2-D FDTD grid of Fig. 1 with no scatterer. A comparison is shown between the G-TF/SF-computed results and the conventional total-field/scattered-field (TF/SF)-computed results for incident source angles, (a) $\theta_{\text{inc}} = 30°$ and (b) $\theta_{\text{inc}} = 210°$. Results for $\theta_{\text{inc}} = 120°$ are identical to that shown in (a).

PML. The side length (OQ) of the G-TF/SF square boundary enclosing the scatterer is chosen to be $130\Delta$. The back (SR) and right (RQ) sides of the G-TF/SF boundary are modeled at a depth of $44\Delta$ within the PML region.

We model the PEC scatterer within the PML by using exactly the same material constants that are used to model the PEC scatterer in free space. The PML absorbing region is modeled with a quadratic loss scheme ($n = 2$) as described in (10). The reflection coefficient parameter, $R_o$, in (11) is chosen to be $10^{-16}$ or smaller. We also note that in order to accurately model either an infinite 45°-angle PEC or dielectric wedge, we require a thicker PML absorbing region with a more gradual loss gradient compared to the PML region required to model the infinite right-angle material wedge.

We now compare the G-TF/SF-computed diffraction coefficients using the method described in [3] for the infinite 45°-angle PEC wedge with the well-known asymptotic diffraction coefficients [4], [5] arising in the uniform theory of diffraction (UTD). Fig. 7 shows the G-TF/SF-computed and UTD-computed diffraction coefficient results for the infinite 45°-angle PEC wedge vertex A, at point E located at ($\rho = 50.99\Delta x$, $\phi = 191.31°$) relative to vertex A, when

the plane-wave is incident at $\theta_{\text{inc}} = 30°$ and $\theta_{\text{inc}} = 120°$. When compared to the UTD-computed asymptotic results in the frequency range of 100–1000 MHz, these G-TF/SF results show less than 3% error. The good correspondence of our numerical diffraction coefficients with asymptotic results for the infinite 45°-angle PEC wedge indicates the probable validity of our method for arbitrary-angle wedges. We note that, even with the requirement to have a $48\Delta$-thick PML for this worst case example which requires a slower loss gradation in the PML, the total grid size for a 3-D problem is expected to be about $185 \times 185 \times 185$ cells. This can be implemented handily with current personal computers having 0.5 GB or more of ramdom-access-memory (RAM).

### B. Numerical Results for an Infinite 90° Dielectric Wedge

In this section, we present numerical results for the 2-D TM diffraction of the infinite right-angle dielectric ($\varepsilon_r = 5$) wedge modeled using the very compact geometry shown in Fig. 8. The infinite dielectric wedge is modeled as a finite square cylinder with a side length of $40\Delta$ in free space. The left (AB) and front (AD) sides of the square cylinder extend into the PML absorbing
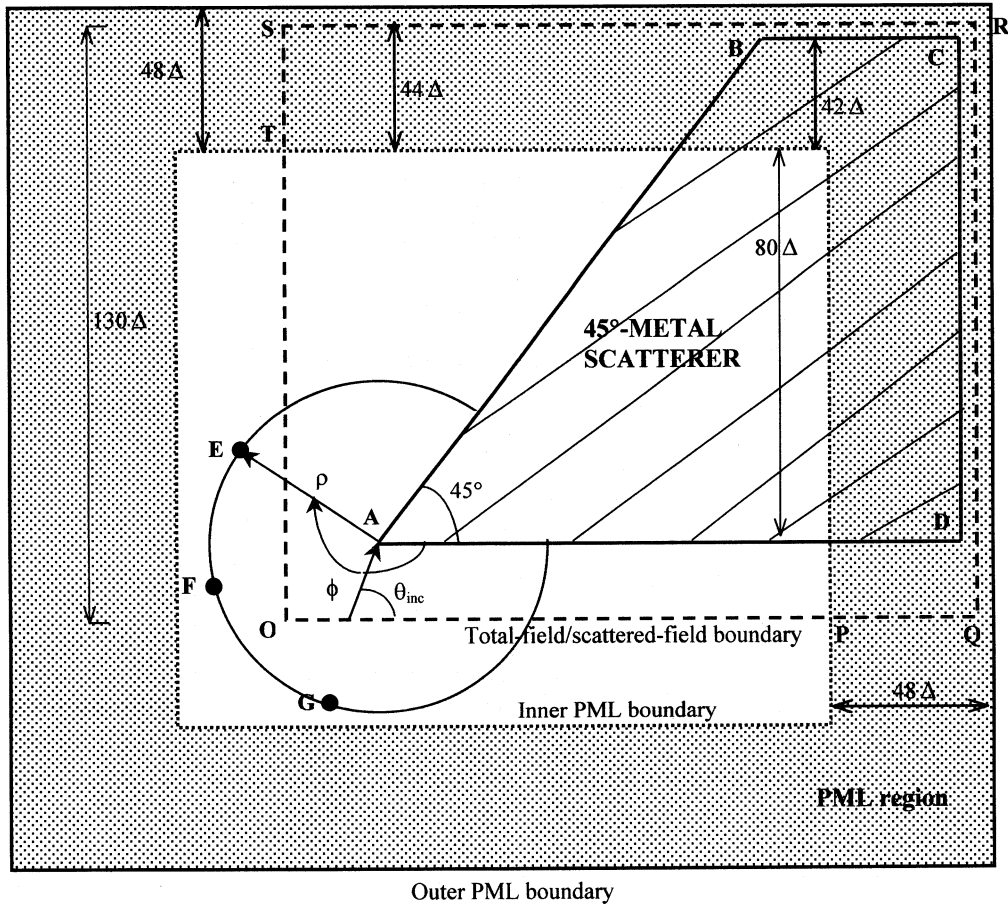
Fig. 6.   Infinite 2-D 45°-angle perfect-electrical-conductor (PEC) wedge modeled in a FDTD grid using the G-TF/SF formulation. Observation points E, F, and G are in the scattered field region. This figure is not drawn to scale.
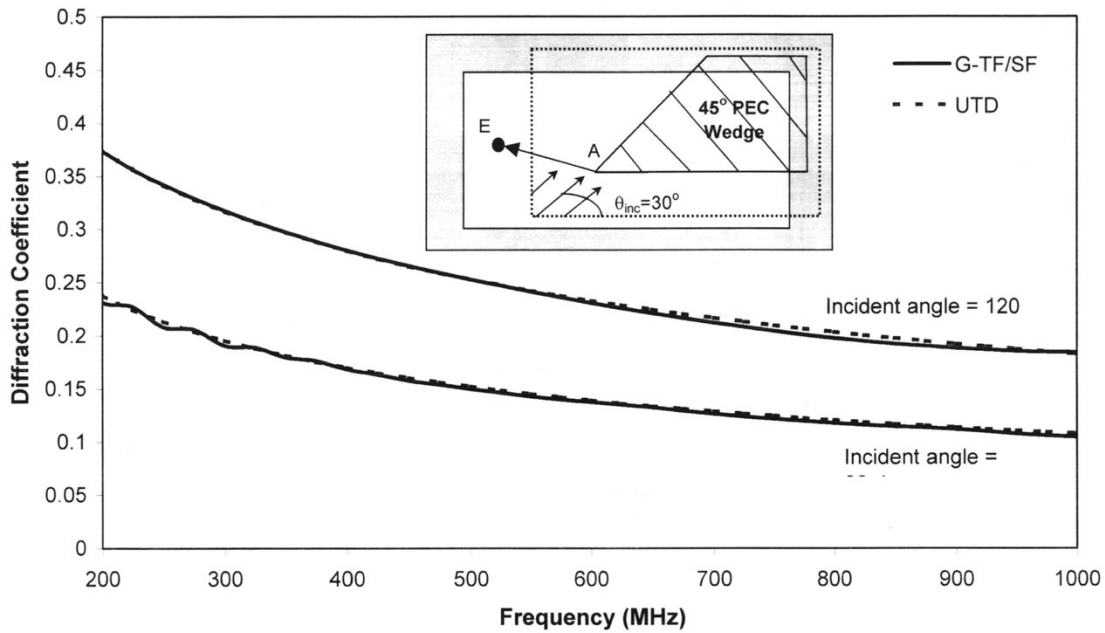


Fig. 7.   Diffraction coefficients of the infinite 2-D 45°-angle PEC wedge at observation point E, located at ($\rho = 50.99\Delta x$, $\phi = 191.31°$) relative to vertex A, when the plane-wave is incident at $\theta_{\mathrm{inc}} = 30°$ and $\theta_{\mathrm{inc}} = 120°$. Numerical G-TF/SF-computed results are compared to the asymptotic results of UTD.

region up to a PML depth of $10\Delta$. Thus, the back (BC) and right (CD) sides of the cylinder lie at a depth of $10\Delta$ inside the PML absorbing region. The side length (OQ) of the G-TF/SF square boundary enclosing the cylinder is chosen to be $57\Delta$. The back
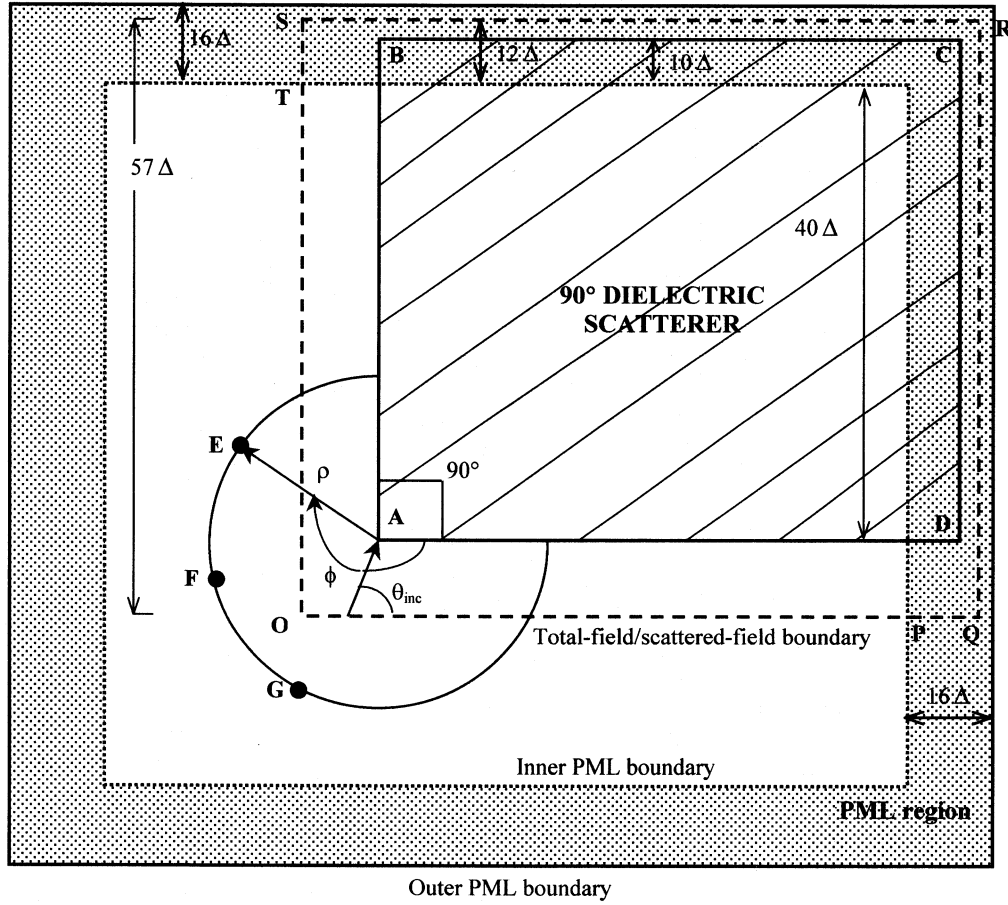
Fig. 8. Infinite 2-D right-angle dielectric wedge modeled in a compact FDTD grid using the G-TF/SF formulation. Observation points E, F, and G are in the scattered field region. This figure is not drawn to scale.

(SR) and right (RQ) sides of the G-TF/SF boundary are modeled at a depth of $12\Delta$ within the PML region.

We model the lossless dielectric cylinder within the PML by using the dielectric constant in the field update equations for the PML and by using the loss grading described by (10). The PML absorbing region is modeled with a quadratic loss scheme ($n = 2$) as described in (10). In order to achieve very accurate results for dielectric scatterers, the reflection coefficient parameter, $R_o$, in (11) is chosen to be $10^{-30}$, or smaller.

Fig. 9 compares the scattered field of the finite dielectric ($\varepsilon_r = 5$) cylinder of Fig. 8 obtained by using the G-TF/SF formulation with the results of the conventional TF/SF formulation. Here, the same compact FDTD grid and the same modulated gaussian impulsive source ($f_o = 850$ MHz, $\Delta f = 600$ MHz) are used for both calculations. Fig. 9 shows the numerical results for the time waveform of the scattered field observed at point E, located at ($\rho = 44.72\Delta$, $\phi = 206.56°$) relative to vertex A of the cylinder, for a plane wave incident at $\theta_{\text{inc}} = 10°$. It is clear from this figure that the G-TF/SF-computed scattered field results contain only the diffracted field (Ⓐ) from vertex A, while the TF/SF-computed results contain the diffracted field (Ⓐ) from vertex A, and the scattered field (Ⓑ and Ⓒ) from the other cylinder sides and vertices. The G-TF/SF result can be used to directly obtain the diffraction coefficient of the corresponding infinite dielectric wedge having vertex A. However, the TF/SF

computed results cannot be used to obtain this diffraction coefficient since the diffracted field of interest (Ⓐ) cannot be isolated in the time-domain in this compact grid. In fact, depending on the incident-wave source angle and the diffracted-wave observation point, the TF/SF-computed result requires the use of a much larger cylinder in a much larger grid to permit time isolation and windowing of Ⓐ. On the other hand, the G-TF/SF model utilizes a compact fixed-size grid.

Fig. 10 compares the numerical diffraction coefficients for the infinite 90° dielectric wedge vertex A obtained by using the compact G-TF/SF grid of Fig. 8 with the results for a much larger cylinder and a much larger grid obtained by using the conventional TF/SF formulation. In order to permit effective time-gating, the scatterer used in the conventional TF/SF formulation is chosen to have a side length of $170\Delta$. Fig. 10 shows a very good correspondence (less than 2% difference) between the G-TF/SF-computed and TF/SF-computed results at point E located at ($\rho = 44.72\Delta$, $\phi = 206.56°$) as shown in Fig. 8, when the plane wave is incident at $\theta_{\text{inc}} = 10°$. For the results shown here, the cylinder size is reduced by about 4 : 1 in each dimension using the G-TF/SF method relative to the conventional TF/SF method. This implies up to a 16 : 1 reduction in computer memory and running time in 2-D and up to a 64 : 1 reduction for 3-D. This demonstrates the advantage of using the G-TF/SF formulation relative to
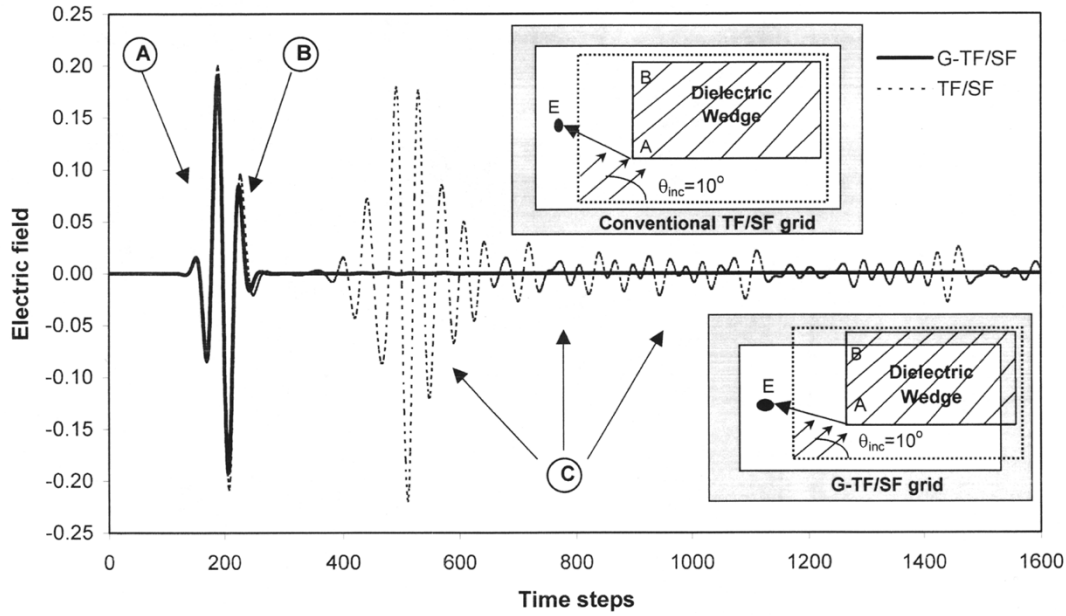
Fig. 9. Comparison of scattered field at point E from the square dielectric ($\varepsilon_r = 5$) scatterer shown in Fig. 7, obtained by using the G-TF/SF formulation and the conventional TF/SF formulation. The response labeled Ⓐ shows the diffracted field from vertex A, Ⓑ shows the field due to vertex B and Ⓒ shows the field due to all the other vertices and edges. The G-TF/SF results contain Ⓐ only, while the TF/SF results contain Ⓐ, Ⓑ, and Ⓒ.
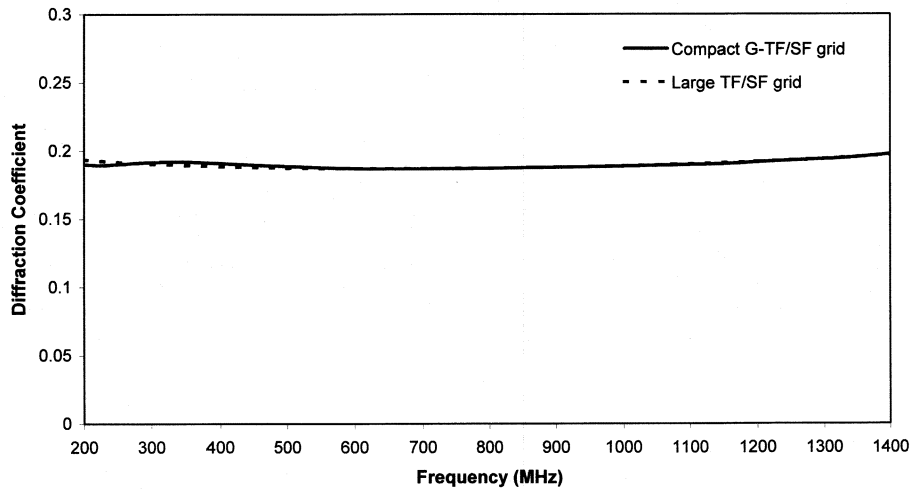


Fig. 10. Comparison between the G-TF/SF-computed and TF/SF-computed diffraction coefficients for the infinite 2-D right-angle dielectric wedge at observation point E, when the plane-wave is incident at $\theta_{\mathrm{inc}} = 10°$. The G-TF/SF results are obtained using the compact grid (Fig. 7), while the TF/SF results are obtained using time-gating with a large grid.

the TF/SF formulation to efficiently model infinite scatterers illuminated by plane waves, especially in 3-D.

## VII. CONCLUSION

This paper proposed a novel G-TF/SF formulation to efficiently model an infinite material scatterer illuminated by an arbitrarily oriented plane wave within a compact FDTD grid. This requires the sourcing of numerical plane waves traveling into, or originating from, the PML absorber bounding the grid. In this formulation, the G-TF/SF boundary is located in part within the PML.

This paper derived the special update equations describing the G-TF/SF boundary. It was shown that the incident fields re-

quired to evaluate the special update equations within the PML can be obtained accurately using FDTD in preliminary calibration runs. Numerical results showed that the G-TF/SF boundary accurately generates wideband plane waves of effectively infinite extent for arbitrary angles of incidence when this boundary lies in part within the PML and even when the wave originates within the PML.

The G-TF/SF formulation was then applied to model 2-D TM diffraction of an infinite 45°-angle PEC wedge and an infinite right-angle dielectric wedge. Numerical results showed that it is feasible to accurately obtain diffraction coefficients in a grid that is much more compact than that required for the conventional TF/SF formulation. The good correspondence of our numerical diffraction coefficients with the well-known asymptotic

results for the infinite 45°-angle PEC wedge indicates the probable validity of our method for arbitrary-angle wedges of infinite extent. In our ongoing research, we are extending this method to 2-D, TE, and 3-D FDTD grids. In 3-D, the G-TF/SF formulation should allow up to 64 : 1 reduction in computer storage and running time for diffraction coefficient calculations relative to the previous TF/SF approach.

REFERENCES

[1] K. R. Umashankar and A. Taflove, "A novel method to analyze electromagnetic scattering of complex objects," *IEEE Trans. Electromagn. Compat.*, vol. 24, pp. 397–405, 1982.

[2] J. P. Berenger, "A perfectly matched layer for the absorption of electromagnetic edtoolswaves," *J. Comput. Phys.*, vol. 114, pp. 185–200, 1994.

[3] G. Stratis, V. Anantha, and A. Taflove, "Numerical calculation of diffraction coefficients of generic conducting and dielectric wedges using FDTD," *IEEE Trans. Antennas Propagat.*, vol. 45, no. 10, pp. 1525–1529, Oct. 1997.

[4] R. G. Kouyoumjian and PH. Pathak, "A uniform geometrical theory of diffraction for an edge in perfectly conducting surface," *Proc. IEEE*, vol. 62, pp. 1448–1461, Nov. 1974.

[5] C. A. Balanis, "Geometrical theory of diffraction," in *Advanced Engineering Electromagnetics*. New York: Wiley, 1989, ch. 13.

[6] A. Taflove, *Computational Electrodynamics: The Finite-Difference Time-Domain Method*. Norwood, MA: Artech House, 1995, pp. 107–144.

[7] ——, *Computational Electrodynamics: The Finite-Difference Time-Domain Method*. Norwood, MA: Artech House, 1995, pp. 145–202.

[8] ——, *Computational Electrodynamics: The Finite-Difference Time-Domain Method*. Norwood, MA: Artech House, 1995, pp. 203–224.

[9] ——, *Computational Electrodynamics: The Finite-Difference Time-Domain Method*. Norwood, MA: Artech House, 1995, pp. 77–79.

**Veeraraghavan Anantha** was born in Tamil Nadu, India, in 1972. He received the B.S. degree in engineering physics from the Indian Institute of Technology, Bombay, India, the M.S. degree in physics, and the Ph.D. degree in electrical engineering from Northwestern University, Evanston, IL, in 1994, 1996, and 2001, respectively.

From 1996 to 2001, he was with Advanced Radio Technologies, Motorola, Inc., Arlington Heights, IL, working on enhancing the technology used to predict RF propagation for wireless communications in indoor and outdoor urban environments. He has also worked on designing and prototyping third generation cellular base stations and mobile-phone systems. Since 2001, he has been with Intrinsity, Inc., Austin, TX, designing high performance signal processors that enable software implementation of next gernation wirelss systems. His current research interests include the architecture and design of efficient next generation wireless communications systems for local and wide area networking.

**Allen Taflove** (F'90) was born in Chicago, IL, on June 14, 1949. He received the B.S., M.S., and Ph.D. degrees in electrical engineering from Northwestern University, Evanston, IL in 1971, 1972, and 1975, respectively.

For nine years, he was with IIT Research Institute, Chicago, IL, working as a Research Engineer. In 1984, he joined Northwestern University and since 1988, he has been a Professor in the Department of Electrical and Computer Engineering, McCormick School of Engineering. In 2000, he was appointed Director of Northwestern Center for Computational Science and Engineering. Since 1972, he has pioneered basic theoretical approaches and engineering applications of finite-difference time-domain (FDTD) computational electromagnetics, and he coined the FDTD acronym in 1980 in an IEEE paper. He is author or coauthor of 12 invited book chapters, 70 journal papers, approximately 200 conference papers and abstracts, and 12 U.S. patents. He is the author of *Computational Electrodynamics—The Finite-Difference Time-Domain Method* (Norwood, MA: Artech House, 1995), which is now in its second edition, and editor of *Advances in Computational Electrodynamics—The Finite-Difference Time-Domain Method* (Norwood, MA: Artech House, 1998). He was also honored as one of four Charles Deering McCormick Professors of Teaching Excellence at Northwestern and was appointed as the faculty master of Northwestern's Lindgren Residential College of Science and Engineering. He is the faculty advisor to McCormick's Undergraduate Design Competition and advises the student chapter of Eta Kappa Nu and Tau Beta Pi.

Dr. Taflove was named one of the most Highly Cited Researchers by the Institute for Scientific Information (ISI) in January 2002.